Tail-Wave-Assisted Positron Acceleration in Nonlinear Laser Plasma Wakefields

Wei-Yuan Liu,[1,2] Xing-Long Zhu,[1,2,3] Min Chen,[1,2,*] Su-Ming Weng,[1,2] Feng He,[1,2] Zheng-Ming Sheng,[1,2,3] and Jie Zhang[1,2,3]

[1] *Key Laboratory for Laser Plasmas (MOE), School of Physics and Astronomy, Shanghai Jiao Tong University, Shanghai 200240, China*

[2] *Collaborative Innovation Center of IFSA (CICIFSA), Shanghai Jiao Tong University, Shanghai 200240, China*

[3] *Tsung-Dao Lee Institute, Shanghai Jiao Tong University, Shanghai 200240, China*

(Received 17 July 2022; revised 5 January 2023; accepted 14 March 2023; published 18 April 2023)

Relativistic laser-wakefield acceleration is characterized by an unsurpassed accelerating gradient, which is very suitable for electron acceleration over short distances and could be a promising candidate for next-generation compact accelerators. However, using this technique for positron acceleration remains challenging because positively charged particles are commonly defocused in the accelerating structure of a standard nonlinear wakefield driven by an ultrashort laser pulse. Here we propose and numerically demonstrate a scheme to accelerate an externally injected positron beam in a nonlinear laser wakefield in a regime where a tail wave is formed behind density cusps of the wakefield. This tail wave can provide a focusing force in addition to longitudinal acceleration for the positrons. Three-dimensional particle-in-cell simulations demonstrate that a trapping efficiency of positrons of nearly 100% in the nonlinear wakefield is possible. This scheme may open a simple way to achieve compact positron acceleration of hundreds of MeV at high repetition rates with terawatt-class laser systems without the need for special laser modes and plasma structures.

DOI: 10.1103/PhysRevApplied.19.044048

I. INTRODUCTION

Plasma-based acceleration has become an active research area in recent years due to its extremely high acceleration gradient and potential application for the next generation of compact accelerators [1,2]. They are capable of supporting an acceleration gradient exceeding 100 GV/m, which is several orders of magnitude higher than those in conventional accelerators. In the nonlinear regime of laser-wakefield acceleration (LWFA) or plasma-wakefield acceleration (PWFA), a relativistically intense drive laser or dense charge-particle bunch excites a bubblelike electron cavity [3,4]. This structure is inherently suitable for efficient acceleration of electrons, because electrons can be focused and accelerated simultaneously in a region covering half of the wake. This has spurred rapid progress of wakefield acceleration and its applications in the last four decades [5]. However, positrons, the antiparticle of the electrons, are generally defocused by the transverse field in the bubble of the nonlinear wakefields, making it quite difficult to achieve effective positron acceleration. Positrons at high energies of several hundred MeV to TeV are widely used in fields such as laboratory astrophysics [6–9] and lepton colliders [10–12]. Currently, they still rely on huge size accelerators. The realization of positron acceleration in a university-scale laboratory would be stimulating and of milestone significance in popularizing positron-based applied research.

Significant efforts have been made towards this goal in both PWFA and LWFA. Recently, a hollow electron beam [13] or a positron beam [14,15] as the driver and an electron beam in a finite-radius plasma column [16] were proposed to form an on-axis filament of plasma electrons to create a broad region in the wake cavity that focuses and accelerates positrons simultaneously. Besides, a wake excited by an electron beam in a hollow plasma channel was proposed for positron transport under zero defocusing force inside the channel [17–19]. Despite these advances, these methods still rely on tens of GeV dense particle beams, which are only accessible in few large conventional accelerator facilities. By contrast, LWFA is appealing due to its compact size, low cost, and flexible beam time. In LWFA, a Laguerre-Gaussian (LG) laser pulse is suggested to drive the self-injection of the donutlike electrons and form the positron focusing region [20]. Although this scheme is quite promising, it requires high-intensity LG lasers, which is more difficult to achieve than usual Gaussian lasers. Thus, configurations for positron acceleration in wakefields driven by a usual Gaussian laser is highly desirable.

*minchen@sjtu.edu.cn

In this work, we propose and numerically demonstrate that an extended region favorable for positron focusing and acceleration can be created in the nonlinear wakefield driven by a laser pulse with a transverse Gaussian profile. We show that when the laser intensity is marginally beyond the threshold for the nonlinear wakefields, where self-injection of electrons is not significant, a large number of plasma electrons near the density cusp at the rear of the first wave bucket behind the laser pulse can traverse the second bubble. They can form a tail wave other than composing the following wake, and some tail-wave electrons can converge into an on-axis high-density filament in the bubble. Compared to previous schemes to accumulate electrons, the tail wave does not rely on special modulations of the laser mode and plasma structure, which greatly reduces the experimental difficulty. Moreover, when a positron beam is externally injected into the accelerating phase of such wakefields, more tail-wave electrons near the positron beam can be dragged towards the beam, as shown in Fig. 1. Such a structure enables efficient focusing and acceleration of the loaded positron beam. We call this scenario "tail-wave-assisted positron acceleration" (TWAA).

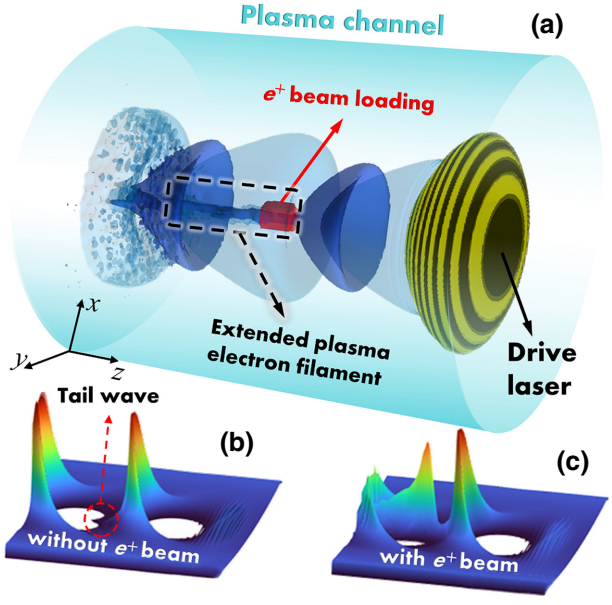

FIG. 1. Sketch of the positron-acceleration scheme. (a) A drive laser (yellow-black) and trailing positron beam (red) propagate in a parabolic plasma channel (light blue). (b) When there is no positron loaded, only a small cluster of electrons near the bubble boundary is gathered on the axis to form a tail wave. (c) When a positron beam is loaded, the tail wave is magnified with a high-density electron filament formed around the axis in the second plasma wave bucket behind the drive pulse.

II. SIMULATION RESULTS AND DISCUSSION

We simulate such an acceleration process by using three-dimensional particle-in-cell (3D PIC) simulations with OSIRIS code [21] that has been equipped with the charge-conserving current depositing methods [22,23] and the field solver is done locally using a finite-difference solver for the electric and magnetic fields in both space and time [24]. A linearly polarized laser is used to drive a nonlinear wake in a preformed plasma channel. To be convenient, we introduce co-moving frame variables $(x, y, \xi = z - ct, t)$, with (x, y) being the transverse coordinates $(r = \sqrt{x^2 + y^2})$, t, c, and z being the time, the speed of light, and the longitudinal coordinates, respectively. The spatiotemporal profile of the laser is given by $\boldsymbol{a} = a_0 \exp(-r^2/w_0^2)\sin^2(\pi t/2\tau_0)\mathbf{e}_y$, where a_0 is the peak vector potential of the laser, w_0 is the spot size, τ_0 is the FWHM duration. The plasma channel has a parabolic transverse density profile

$$n_e = n_{e0} + \Delta n r^2/r_0^2, \tag{1}$$

where n_{e0} is the on-axis electron density, r_0 is the channel width, and $\Delta n = (\pi r_e r_0^2)^{-1}$ is the channel depth with $r_e = e^2/m_e c^2$ the classical electron radius. The simulation box has a size of $40\lambda_0(x) \times 40\lambda_0(y) \times 80\lambda_0(z)$, divided into $200 \times 200 \times 2400$ grid cells with two macroparticles per cell for the plasma electrons (ions) and eight macroparticles per cell for the positrons.

We first study the tail-wave characteristics without loading positrons. Figure 2 shows the simulation results using a laser pulse with $a_0 = 1.6$, $w_0 = 12\lambda_0$, $\tau_0 = 7.5T_0$ ($T_0 = \lambda_0/c$ is the laser period). Considering the laser wavelength $\lambda_0 = 1$ μm, it corresponds to a laser with energy of 150 mJ, peak power of 8 TW, and peak intensity of 3.5×10^{18} W/cm^2. Comparable parameters can be obtained at the commercial kHz laser systems [25]. The laser pulse propagates in a plasma channel with $r_0 = w_0$ and $n_{e0} \approx 4 \times 10^{18}$ cm^{-3} (giving the critical power for relativistic optical guiding $P_c \simeq 5$ TW) [26]. Since $P > P_c$, relativistic self-focusing also contributes to the guiding of the drive laser; hence the competition between the ponderomotive potential of the driver and the radial focusing field of the wake is evolving as the laser propagates. This leads to the modification of electron trajectories behind the laser, resulting in three types of the tail wave being formed at different stages. In response to a lower-intensity drive laser, most electrons with initial transverse coordinates smaller than the laser spot size can slip into the second bubble without apparent oscillations because of the weaker plasma perturbation; and the plasma wave front where the electron density peaks is curved due to the slightly longer plasma wavelength $\lambda_{Np} \propto \sqrt{|\boldsymbol{a}|/n_e}$ on axis than off axis [called tail wave I, see Fig. 2(a)]. This allows a limited region behind this peak to hinder the positron defocusing [see the

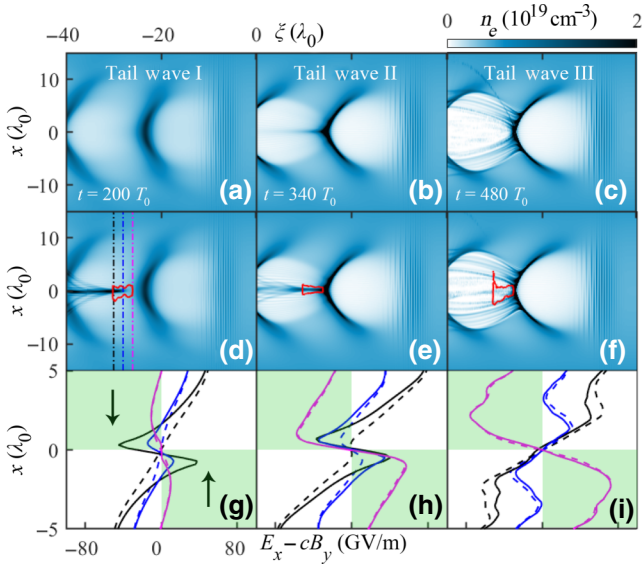

FIG. 2. Snapshots of electron-density distributions (white-blue gradients) in ξ-x plane show different patterns of tail waves in unloaded wakefields [(a)–(c)] and positron loaded wakefields [(d)–(f)]. The red solid line denotes the one-tenth contour of the initial positron density. (g)–(i) Slices of transverse field $E_x - cB_y$ along the x axis at the back edge (black), the centroid (blue), and the front edge (magenta) of the positron beam. The results in the unloaded case and the positron loaded case are denoted by the dashed lines and solid lines, respectively. The green shadings indicate the region where positrons can be transversely focused and the arrows represent the force direction.

magenta dashed line in Fig. 2(g)]. As the laser intensity increases moderately, electron accumulation and curvature at the plasma wave front are enhanced and some off-axis electrons gather at the vicinity of the central axis of the second bubble, forming a high-density filament [called tail wave II, see Fig. 2(b)]. As a consequence, the region suitable for positron focusing is expanded to approach half of a bubble [see Fig. 2(h)]. At a later time, when the laser intensity increases further and electrons are transversely over accelerated, these tail-wave electrons are split transversely [called tail wave III, see Fig. 2(c)]; thus the focusing field for positrons exists only in the axially receding and squeezed density cusp [see Figs. 2(i)] [27].

The dynamics of tail waves can be further modified when a witness positron beam is loaded. Once a positron beam is encompassed by plasma electrons, it spontaneously attracts electrons inward to maintain the charge neutrality [28]. When the plasma density is uniform, the net focusing force of the positron beam on electrons has a linear dependence on the electron density [29]. Similarly, for a positron beam propagating in the tail wave, the transverse sucking is positively correlated with the density of the tail-wave electrons within "reach" of the beam. To investigate such effects, a cylindrical positron beam (i.e., length of $L_+ = 4\lambda_0$ and transverse radius of $r_+ = 2\lambda_0$) with a uniform density of $n_{+0} = 0.5n_{e0}$ (corresponds to an initial charge of $Q_{+0} = 16$ pC) and an initial energy of 20 MeV follows the drive laser and is placed in the second bubble (the back edge of the beam is $\xi_{+,l} = -30\lambda_0$ where the longitudinal electric field $E_z \approx 0$). Other laser and plasma parameters are the same as those mentioned above. As can be seen in Figs. 2(d)–2(f), due to the relaxation time for the electrons in the off-axis tail wave to reach the positron beam [30], a significant enhancement of the on-axis electron density occurs only when the tail waves are formed at stage I and II. Therefore, the transverse field in the front of the beam makes little difference whether positrons are loaded or unloaded, whereas in the rear of the beam it can be turned from a defocusing field to a focusing field as long as the combined electron density of the original on-axis tail-wave electrons and the sucked-in electrons is high enough to exceed the background ion density [see Figs. 2(g)–2(i)]. In general, the focusing strength is proportional to the beam current, thus the elongated electron filament does not provide a uniform focusing strength along different ξ [28], which leads to the inhomogeneous compression over the length of the beam [see Figs. 2(d) and 2(e)]. Meanwhile, because positrons in this example are relativistic with $\gamma_+ > \gamma_p$, where γ_+ and $\gamma_p \simeq \omega_0/\omega_p$ (ω_0 is the laser frequency and ω_p is the plasma-wave frequency) are the Lorentz factor of the beam and the plasma wave, respectively, they slowly move forward while the density of ambient tail-wave electrons gradually increases. This is beneficial for trapping more positrons, not just the first half of the beam. When tail wave III occurs, most positrons in the rear part of the beam are accelerated transversely [see Fig. 2(f)], which results in the potential loss of some accelerated positrons. Fortunately, when the laser is continuously guided in the channel, the laser intensity is decreased [see the black dashed line in Fig. 3(a)] so that tail wave III can gradually revert to tail wave II and tail wave I. As a result, the on-axis electron filament in the positron region is recovered and thus the positron loss ceases. Although about 60% positrons are finally trapped [see the red dashed line in Fig. 3(b)], it is preferable to avoid tail wave III to achieve a more stable positron acceleration.

The blue dashed line in Fig. 3(a) shows the minimum on-axis electron density in the first bucket behind the driver $n(0)/n_{e0}$ in the example, which is used to describe the blowout level of the plasma electrons. It varies with the tail-wave patterns. At the tail wave I and II stages, typically there are $n(0)/n_{e0} \gtrsim 0.2$ and $0.1 \lesssim n(0)/n_{e0} \lesssim 0.2$, respectively, whereas there is $n(0)/n_{e0} \lesssim 0.1$ for tail wave III. Because $n(0)/n_{e0} = 1 - (4/k_p^2 w_0^2)a_\perp^2/(1 + a_\perp^2)^{1/2}$ [31], it is possible to keep $n(0)/n_{e0} \gtrsim 0.1$ throughout the wakefield generation by optimizing the initial laser-plasma parameters. We notice that when a light pulse propagating in a parabolic plasma-channel profile, the

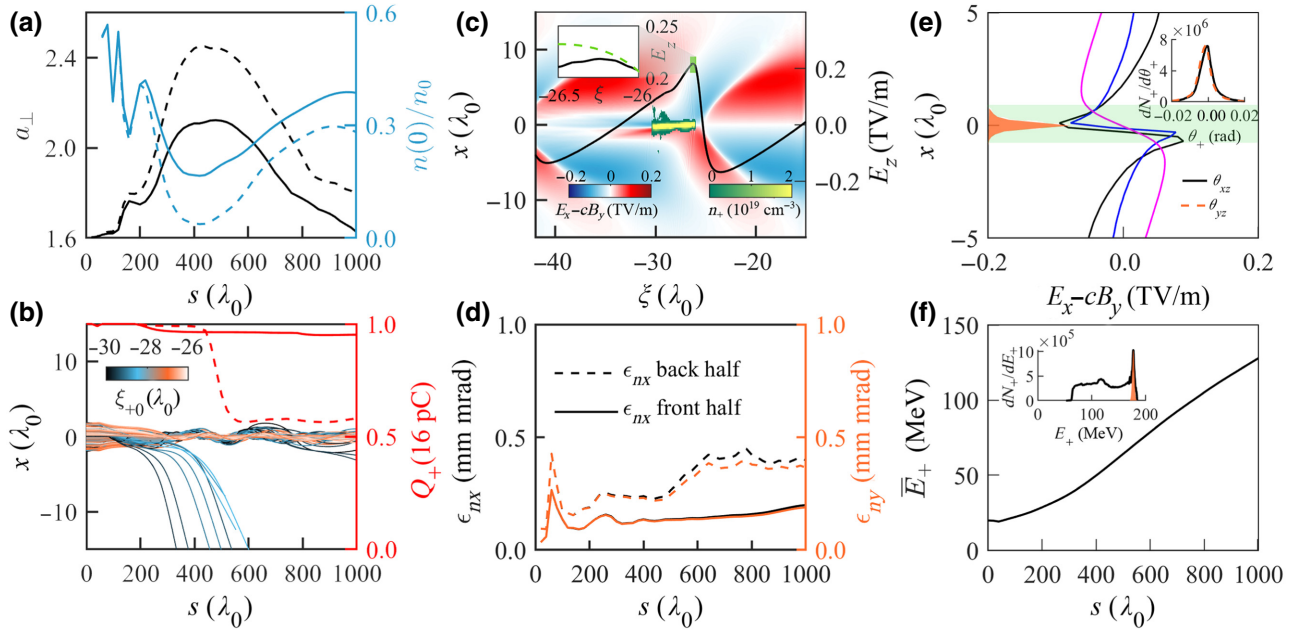

FIG. 3. (a) Evolution of the peak laser vector potential (black) and the minimum on-axis electron density in the first bubble (blue). The solid and dashed lines denote the case with plasma-channel radius $r_0 = 14\lambda_0$ and $r_0 = 12\lambda_0$, respectively. (b) Positron trajectories for the case with $r_0 = 14\lambda_0$ (colors representing the initial longitudinal locations of positrons). The red lines show the evolution of the total charge of the trapped positrons in the cases with $r_0 = 14\lambda_0$ and $r_0 = 12\lambda_0$. (c)–(f) Results for the case with $r_0 = 14\lambda_0$. (c) Transverse field ($E_x - cB_y$, blue-red gradients), positron density (n_+, green-yellow gradients), and longitudinal field slice along $r = 0$ (E_z, solid line) at an acceleration length of $s = 500\lambda_0$. The inset is an enlargement of E_z near its peak, showing both the case of unloaded (green dashed) and loaded (black solid) positron beam. (d) Normalized transverse emittance ϵ_{nx} (black) and ϵ_{ny} (orange) at the back half (dashed line) and the front half (solid line) of the positron beam as a function of s. (e) Transverse fields at three different locations: $\xi = -30\lambda_0$, $\xi = -28\lambda_0$, and $\xi = -26\lambda_0$. The orange shading shows the location and the transverse shape of the positron beam, and the green shading indicates the focusing field of the beam. The inset shows the final angular distribution $\theta_{xz} = p_x/p_z$ (black) and $\theta_{yz} = p_y/p_z$ (orange) of the beam. (f) Evolution of the average energy of positrons. The inset shows the final energy spectrum of the beam, where the orange shading is the symmetric Gaussian fit to the peak $E_+ \approx 177$ MeV.

index of refraction in the plasma channel satisfies [32]

$$\eta \simeq 1 - \frac{\omega_p^2}{2\omega_0^2}\left(1 + \frac{\Delta n}{n_0}\frac{r^2}{r_0^2} + \frac{\delta n}{n_0} - \frac{a_0^2}{8}\right). \qquad (2)$$

If one increases the channel radius and makes sure $r_0 > w_0$, the effects of relativistic self-focusing will be weakened as η increases. For this purpose, we adopt a wider plasma channel with $r_0 = 14\lambda_0$ and keep other parameters the same as those in Fig. 2(d). Due to the limited increase of the laser intensity [see the black solid line in Fig. 3(a)], only I and II type tail waves are excited in this case because $n(0)/n_{e0}$ is increased compared to that in the case of $r_0 = 12\lambda_0$ [see Fig. 3(a)]. Accordingly, more efficient positron trapping is successfully achieved, where more than 95% of the initial charge can be accelerated after a propagation distance of $s = 1000\lambda_0$ [see the red solid line in Fig. 3(b)]. The 5% positron charge loss originates mainly from the latter middle area of the beam during the stage of tail wave I [see Fig. 3(b)], which is caused by the delayed transition of the tail-wave pattern due to the weakened laser focusing. Note that the evolution time scale of positrons is the betatron period $\tau_\beta = 2\pi\sqrt{\gamma_+/[dE_r/dr]_{E_r=0}}$ [33], where dE_r/dr is the slope of the transverse field and it varies with ξ. As a result, positrons with different longitudinal positions are in different phases of the oscillations for a given s and the front ones have a more stable acceleration [see Fig. 3(b)]. Since the focusing field is prolonged during the acceleration due to the accumulated electrons, the charge loss is limited.

To study the stability of the positron beam, we show in Figs. 3(c) and 3(e) the details of the focusing field and the positron density at a propagation distance of $s = 500\lambda_0$ when the laser intensity reaches its maximum. In addition, the evolution of the normalized transverse emittance of the positron beam along different directions, i.e., ϵ_{nx} and ϵ_{ny}, is illustrated in Fig. 3(d). As one can see, the focusing field for positrons is extended to a length nearly occupying the whole second wake bubble. The slight asymmetry in the focusing field at the rear of the positron beam is due to the positron loss at an earlier moment. Although this potentially induces the tail instability of the beam, it can be damped due to the longitudinal inhomogeneity of the focusing force [34]. As shown in Fig. 3(d), the

growth of ϵ_{nx} and ϵ_{ny} in separate parts of the beam are both quite limited. It increases by 0.26 mm mrad (0.42 mm mrad) in the front (back) part of the beam at the early stage, while decreases by 0.17 mm mrad (0.25 mm mrad) when a stronger focusing field is generated. After that, the emittance of the front part almost saturates, and the back part increases briefly due to the tail instability, but it can also reach saturation when it moves to the interval between the first and second bubble [27]. On the other hand, the transverse focusing region at the back part of the beam is smaller [see Fig. 3(e)], which leads to the formation of a beam halo, where the positrons are compressed at the center and less dense at the periphery [35] [see Fig. 3(c)], the transverse size of the positron beam is reduced to about one third of its original size, and the number density is increased by tens of times. Accordingly, the FWHM divergence of the angular distribution of the beam at $s = 1000\lambda_0$ reaches only $\Delta\theta_{xz} = \Delta\theta_{yz} = 7$ mrad [see the inset of Fig. 3(e)].

To study the positron acceleration, we show the longitudinal field of the wake at $s = 500\lambda_0$ and the beam parameters at $s = 1000\lambda_0$ in Figs. 3(c) and 3(f), respectively. Results of longer acceleration distances can be found in Appendix A. As mentioned before, the positron beam is loaded in the region of $\partial E_z/\partial z > 0$ [see Fig. 3(c)] and it can gradually move forward, thus the average energy gain of the beam increases at a growing gradient with $\Delta\bar{E}_+ \approx 110$ MeV at $s = 1000\lambda_0$ [see Fig. 3(f)]. Although the increase of E_z is destined to cause a large energy spread of the full beam [see the inset of Fig. 3(f)], the high density of the positrons at the most front of the beam makes E_z relatively uniform in a limited region near its peak [see the inset of Fig. 3(c)], and when more positrons enter into the interval with $\partial E_z/\partial z < 0$, the wake naturally provides energy chirp compensation for the positrons [36], which thus leads to an energy peak in the high-energy part. As shown in Fig. 3(f), there is a peak of $E_+ \approx 177$ MeV, the FWHM energy spread of the peak is 3%, and the positron charge contained in this peak is about 2 pC, which is about 1/8 of the initial beam charge. Both the energy spread of the full positron beam and the quasimonoenergetic peak charge can be optimized, see more details in Appendix A.

We also study the validity of the TWAA scheme under different initial parameters. Figures 4(a) and 4(b) present the trapping efficiency and energy gain of the finally accelerated positrons where the intensity a_0 and the focal spot w_0 of the drive laser are varied, respectively. The initial position of the back end of the positron beam is $\xi_{+,l} \approx -3/2\lambda_{Np}(0)$, and other parameters are the same as those in Fig. 2(a). As aforementioned, the tail-wave pattern correlates with the laser intensity. Thus, by decreasing a_0, the positron trapping can be enhanced, albeit at the cost of the acceleration gradient due to $E_z \propto a_\perp^2/\sqrt{1+a_\perp^2}$, as shown in Fig. 4(a). When $a_0 < 1.6$, more than half of the positrons

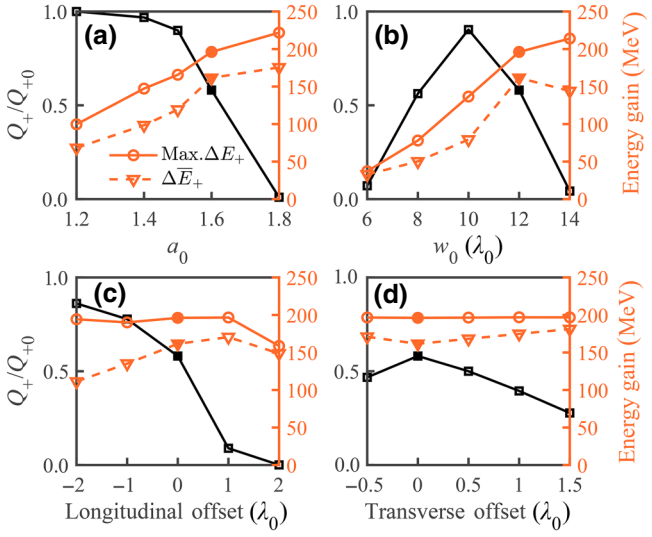

FIG. 4. Variations of the trapping efficiency Q_+/Q_{+0} (black, square markers), maximum energy gain (orange, circular markers), and average energy gain (orange, triangular markers) of the finally accelerated positrons at $s = 1000\lambda_0$ with respect to the parameters of the laser a_0 (a), w_0 (b) and of the positron beam, i.e., different longitudinal (c) or transverse offsets (d) of the beam, respectively. The results of the reference case are marked by solid points. Corresponding data can be found in [37].

can be trapped and accelerated with the acceleration gradient $G \sim 100$ GV/m. When $a_0 = 1.8$, the laser is focused to $a_\perp \approx 3$ and an electron-free cavity is formed such that positrons are almost evacuated before tail wave II is recovered. The positron trapping can also be enhanced by lowering w_0 to the region of $8\lambda_0$ to $12\lambda_0$, as shown in Fig. 4(b). This is attributed to the weakening of the laser focusing by a wider plasma channel, because $\Delta n_c \propto w_0^{-2}$, which leads to the increases of η. The acceleration gradient, depending on the laser focusing, has a tendency to increase with w_0. Note that when w_0 is over reduced, the laser is quickly diffracted, so the positron trapping is restricted. The simulation results for different longitudinal or transverse offsets of the initial positron beam position are also illustrated in Figs. 4(c) and 4(d) relative to the positron beam presented in Fig. 2(d). Longitudinally, the earlier loading within $2\lambda_0$ has no influence on the maximum energy gain, but the trapping ratio is increased and the average energy gain decreases. In contrast, if the positron loading is delayed, the trapping ratio decreases rapidly. This is because the further away from the density spike of the plasma wave front, the lower the electron density. When the positron beam has an initial transverse displacement, positrons are drawn from off axis towards the driver axis $r = 0$, during this process, the hosing instability is caused and induces the growth of the emittance of the positron beam. Despite this, the emittance can be damped when the beam moves into the interval between the first and second bubble (see

more details in Appendix C). Accordingly, there is a trapping tolerance range of $|X_{+0}| \lesssim 0.5\lambda_0$, where X_{+0} is the initial centroid of the beam, the positron loss induced by the increases of the beam emittance is less.

III. CONCLUSION

In conclusion, we propose and numerically demonstrate that positrons can be well accelerated and focused in the tail wave formed behind the density cusp of a nonlinear wakefield driven by an usual Gaussian laser pulse. The trapping efficiency can be close to 100% when the self-focusing effect of the drive laser is weakened by using a plasma channel with a relatively large radius. This TWAA scheme is viable in a certain range of parameters, which shows its feasibility for realistic operation. Furthermore, since this regime requires only drive laser pulses with 10-TW scale, it may be realized with high repetition rate by using kHz laser systems, which makes it very promising for applications requiring hundreds of MeV positron beams.

ACKNOWLEDGMENTS

This work is supported by the National Key R&D Program of China (Grant No. 2018YFA0404802), the National Natural Science Foundation of China (Grants No. 12225505, No. 11991074, No. 12135009, and No. 12205186) and the National Postdoctoral Program for Innovative Talents (Grant No. BX20220206). The authors would like to thank the Supercomputer Center at SJTU for providing computing resources.

APPENDIX A: FEASIBILITY OF OPTIMIZING THE BEAM CHARGE AND THE ENERGY SPECTRUM

In this section, the optimization of the beam charge and the energy spectrum through modifying the initial parameter of the positron beam is further investigated. By increasing the initial positron density [other parameters are the same as Fig. 3(f)], the total charge of the trapped positrons is shown to increases with n'_{+0} in a certain range (see the gray line in Fig. 5). The maximum charge of $Q_+ = 88$ pC is obtained at $n'_{+0} = 8n_{+0}$, which is nearly 6 times the number of the reference case in Fig. 3(b). But one can also note that the trapping efficiency is sacrificed as n'_{+0} increases (see the black line in Fig. 5). This is because an increase in n'_{+0} leads to a stronger inward attraction of the tail-wave electrons, resulting in a growth in the nonuniformity of the density of the electron filament around the positron beam axis. This nonuniformity may cause local electron densities to exceed positron densities, inducing an increase in transverse emittance of positrons and potentially causing some of them to be lost. Besides, the enhancement of on-axis electron aggregation will weaken the acceleration field

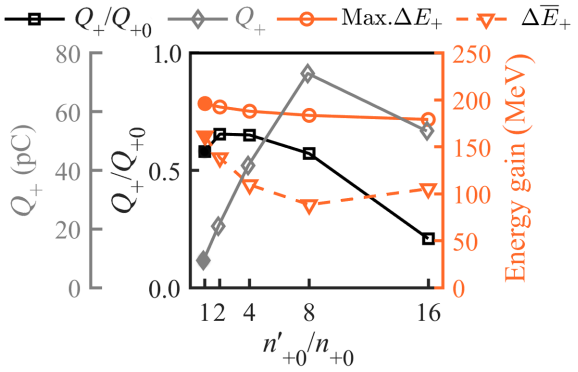

FIG. 5. Variations of the trapping efficiency Q_+/Q_{+0} (black, square markers), the charge Q_+ (gray, diamond markers), the maximum energy gain (orange, circular markers), and the average energy gain (orange, triangular markers) of the finally accelerated positrons at $s = 1000\lambda_0$ with respect to the initial density of the positron beam. Other parameters are the same as those in Fig. 3(f). The results of the reference case are marked by solid points. Corresponding data can be found in [37].

and even cause it to partially convert into a deceleration field. As Fig. 2 shows, the modification in the tail-wave dynamics due to positron loading mainly occurs at the tail beam. Thus, the maximum energy does not evolve obviously as n'_{+0} increases. Meanwhile, in the case of more than 50% of the positron beam is trapped, the average energy decreases with n'_{+0}, while it slightly rebounds when the positron trapping is less than 50% (see the orange lines in Fig. 5).

Moreover, we attempt two methods to optimize the energy spectrum of the injected positron beam. First, replacing the positron bunch into a density asymmetrically distributed one to get a wider range of flattened acceleration field. We set the beam density to a semi-Gaussian distribution, which is experimentally achievable [38], e.g., $n'_{+0} = 6n_{+0}\exp[-(x+26)^2/(2\times 1.77)]$. As shown in Fig. 6, in this case there is a remarkable peak at a lower energy of $E_+ = 90$ MeV, which is due to the stronger beam loading in the front than in the rear of the beam [see Fig. 6(b)]. The positron charge contained in the FWHM of the peak is nearly 10 pC, (about 23% of the total beam charge), which is 5 times larger than that in Fig. 3(f).

As a second method, we exploit the energy-chirp compensation in the wakefields. When the acceleration length is close to the dephasing length, the asymmetric acceleration along the bunch naturally leads to the compensation of the linear energy chirp [36]. It can be observed that when the positron beam continues to propagate in the wakefields, another quasimonoenergetic peak forms in the low-energy part, as Fig. 7 shows. There are 4 and 2 pC contained in the FWHM region of the peak $E_+ = 162$ MeV and $E_+ = 244$ MeV, respectively. Better optimization of the energy spectrum requires more precise adjustment of the

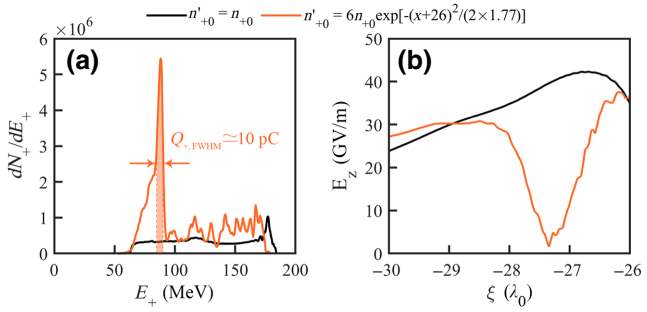

FIG. 6. (a) Energy spectra of the positron beam at the propagation distance of $s = 1000\lambda_0$, where the black line is the same as the inset of Fig. 3(f), the orange line is the result of the case of $n'_{+0} = 6n_{+0}\exp[-(x+26)^2/(2\times 1.77)]$, and the orange shading indicates the FWHM region near the peak $E_+ = 90$ MeV. (b) Lineouts of the acceleration field along $r = 0$ in the positron region at $s = 1000\lambda_0$.

parameters, which is beyond the scope of this work and will be the subject of future studies.

APPENDIX B: LIMITATION OF TWAA SCHEME BY WAKEFIELD DEPHASING AND LASER PUMP DEPLETION

Because laser wakefield acceleration is also limited by particle dephasing and laser pump depletion, here we discuss their limits in the TWAA scheme. By referring to the scaling laws of the blowout regime in Ref. [32], one can qualitatively predict the dephasing length (L_d) and the pump depletion length (L_{pd}). Substituting the parameters of Fig. 3(f) into $L_{pd} \simeq (\omega_0/\omega_p)^2 L_{\mathrm{FWHM}}$ and

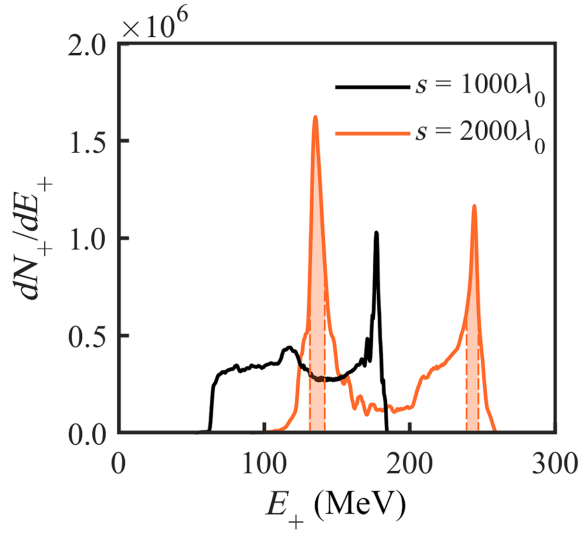

FIG. 7. Energy spectra of positrons at the propagation distance of $s = 1000\lambda_0$ (black) and $s = 2000\lambda_0$ (orange), respectively. The orange shadings represent the FWHM regions of the two peaks.

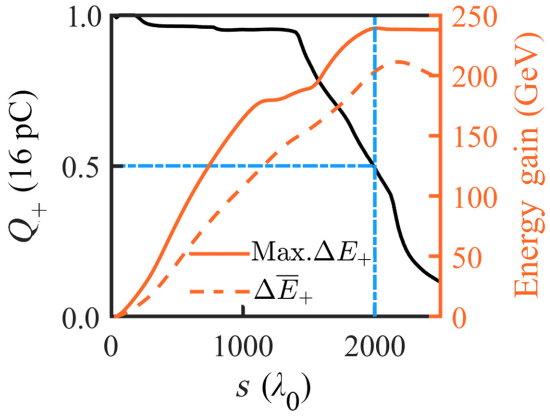

FIG. 8. Evolution of the total charge (black-solid), the gain of the maximum energy (orange-solid), and the average energy (orange-dashed) of the trapped positrons. The vertical and horizontal blue dash-dotted lines represent the propagation distance of and the trapping rate of the positron bunch when the positron acceleration reaches its maximum limit, respectively.

$L_d \simeq (2\omega_0^2/3\omega_p^2)R$, one can get $L_d \simeq 1600\lambda_0$ and $L_{pd} \simeq 4300\lambda_0$. Note that the blowout regime is more nonlinear than the TWAA scheme, thus the actual acceleration length in the TWAA scheme should be longer than the qualitatively predictions limited by the dephasing. This indicates that the effects of dephasing and pump depletion on the TWAA scheme are negligible over the propagation distance of less than $1000\lambda_0$ that is of interest to us in the paper.

A 3D PIC simulation with a longer propagation distance is performed to quantitatively study the limit of positron acceleration. As shown in Fig. 8, at a propagation distance of the positron beam $s = 2000\lambda_0$, positron dephasing causes the first half of the beam to move into the deceleration (also defocusing) region, resulting in the saturation of the maximum energy of the trapped positrons and a loss of 50% of the beam charge, giving max. $\Delta E_+ = 240$ MeV. Prior to this point, the growth rate of max. ΔE_+ experiences a temporary slowdown due to the loss of laser energy in the pump and partial dephasing. However, during this period, the average energy of the trapped positrons continues to increase at a high rate due to the positron loss, resulting in $\Delta\overline{E}_+ = 203$ MeV when 50% of the beam charge is lost.

APPENDIX C: STABILITY OF THE POSITRON BEAM IN THE CASE WITH AN INITIAL TRANSVERSE OFFSET

To evaluate the stability of the positron beam in the case with an initial transverse offset, we study the emittance evolution of the positron beam by changing the initial centroid of the beam with other parameters the same

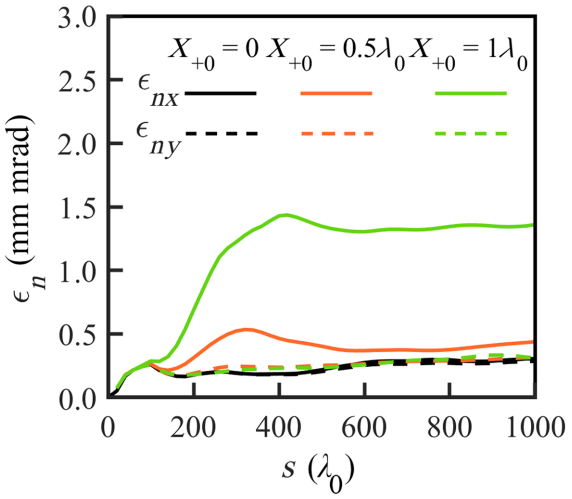

FIG. 9. Transverse emittance evolution in the case of the initial centroid of the positron beam $X_{+0} = 0$ (black), $X_{+0} = 0.5\lambda_0$ (orange), and $X_{+0} = 1\lambda_0$ (green), respectively. Other parameters are the same with Fig. 3(d). ϵ_{nx} and ϵ_{ny} are the solid and dashed lines, respectively.

as Fig. 3(d). As shown in Fig. 9, for the case of different beam centroid, ϵ_{nx} and ϵ_{ny} both can be preserved, which demonstrates that hosing instability reaches saturation, due to naturally occurring head-to-tail variations in the focusing force [34]. Thus, although an initial transverse displacement may seed the hosing instability, it can be damped and saturated in the following acceleration period.

[1] T. Tajima and J. M. Dawson, Laser Electron Accelerator, Phys. Rev. Lett. **43**, 267 (1979).

[2] P. Chen, J. M. Dawson, R. W. Huff, and T. Katsouleas, Acceleration of Electrons by the Interaction of a Bunched Electron Beam with a Plasma, Phys. Rev. Lett. **54**, 693 (1985).

[3] A. Pukhov and J. Meyer-ter Vehn, Laser wake field acceleration: The highly non-linear broken-wave regime, Appl. Phys. B **74**, 355 (2002).

[4] W. Lu, C. Huang, M. Zhou, W. B. Mori, and T. Katsouleas, Nonlinear Theory for Relativistic Plasma Wakefields in the Blowout Regime, Phys. Rev. Lett. **96**, 165002 (2006).

[5] C. Joshi, S. Corde, and W. B. Mori, Perspectives on the generation of electron beams from plasma-based accelerators and their near and long term applications, Phys. Plasmas **27**, 070602 (2020).

[6] G. Sarri, K. Poder, J. M. Cole, W. Schumaker, A. Di Piazza, B. Reville, T. Dzelzainis, D. Doria, L. A. Gizzi, and G. Grittani, *et al.*, Generation of neutral and high-density electron – positron pair plasmas in the laboratory, Nat. Commun. **6**, 6747 (2015).

[7] J. Warwick, T. Dzelzainis, M. E. Dieckmann, W. Schumaker, D. Doria, L. Romagnani, K. Poder, J. M. Cole, A. Alejo, and M. Yeung, *et al.*, Experimental Observation of a Current-Driven Instability in a Neutral Electron-Positron Beam, Phys. Rev. Lett. **119**, 185002 (2017).

[8] C. Boehm, D. Hooper, J. Silk, M. Casse, and J. Paul, MeV Dark Matter: Has it Been Detected?, Phys. Rev. Lett. **92**, 101301 (2004).

[9] T. Ishikawa, H. Fujimura, D. N. Grigoriev, R. Hashimoto, S. Kaida, R. Kitazawa, G. N. Kuznetsov, A. Nakamura, H. Shimizu, and K. Suzuki, *et al.*, Testing a prototype BGO calorimeter with 100–800 MeV positron beams, Nucl. Instrum. Methods Phys. Res. A **837**, 109 (2016).

[10] W. Leemans and E. Esarey, Laser-driven plasma-wave electron accelerators, Phys. Today **62**, 44 (2009).

[11] K. Nakajima, J. Wheeler, G. Mourou, and T. Tajima, Novel laser-plasma TeV electron-positron linear colliders, Int. J. Mod. Phys. A **34**, 1943003 (2019).

[12] W.-Y. Liu, K. Xue, F. Wan, M. Chen, J.-X. Li, F. Liu, S.-M. Weng, Z.-M. Sheng, and J. Zhang, Trapping and acceleration of spin-polarized positrons from γ photon splitting in wakefields, Phys. Rev. Res. **4**, L022028 (2022).

[13] N. Jain, T. M. Antonsen, and J. P. Palastro, Positron Acceleration by Plasma Wakefields Driven by a Hollow Electron Beam, Phys. Rev. Lett. **115**, 195001 (2015).

[14] S. Corde, E. Adli, J. M. Allen, W. An, C. I. Clarke, C. E. Clayton, J. P. Delahaye, J. Frederico, S. Gessner, and S. Z. Green, *et al.*, Multi-gigaelectronvolt acceleration of positrons in a self-loaded plasma wakefield, Nature **524**, 442 (2015).

[15] A. Doche, C. Beekman, S. Corde, J. M. Allen, C. I. Clarke, J. Frederico, S. J. Gessner, S. Z. Green, M. J. Hogan, and B. O'Shea, *et al.*, Acceleration of a trailing positron bunch in a plasma wakefield accelerator, Sci. Rep. **7**, 14180 (2017).

[16] S. Diederichs, T. J. Mehrling, C. Benedetti, C. B. Schroeder, A. Knetsch, E. Esarey, and J. Osterhoff, Positron transport and acceleration in beam-driven plasma wakefield accelerators using plasma columns, Phys. Rev. Accel. Beams **22**, 081301 (2019).

[17] S. Gessner, E. Adli, J. M. Allen, W. An, C. I. Clarke, C. E. Clayton, S. Corde, J. P. Delahaye, J. Frederico, and S. Z. Green, *et al.*, Demonstration of a positron beam-driven hollow channel plasma wakefield accelerator, Nat. Commun. **7**, 11785 (2016).

[18] S. Y. Zhou, J. F. Hua, W. M. An, W. B. Mori, C. Joshi, J. Gao, and W. Lu, High Efficiency Uniform Wakefield Acceleration of a Positron Beam Using Stable Asymmetric Mode in a Hollow Channel Plasma, Phys. Rev. Lett. **127**, 174801 (2021).

[19] T. Silva, L. D. Amorim, M. C. Downer, M. J. Hogan, V. Yakimenko, R. Zgadzaj, and J. Vieira, Stable Positron Acceleration in Thin, Warm, Hollow Plasma Channels, Phys. Rev. Lett. **127**, 104801 (2021).

[20] J. Vieira and J. T. Mendonça, Nonlinear Laser Driven Donut Wakefields for Positron and Electron Acceleration, Phys. Rev. Lett. **112**, 215001 (2014).

[21] R. A. Fonseca, L. O. Silva, F. S. Tsung, V. K. Decyk, W. Lu, C. Ren, W. B. Mori, S. Deng, S. Lee, and T. Katsouleas, *et al.*, in *Computational Science — ICCS 2002*, edited by Peter M. A. Sloot, Alfons G. Hoekstra, C. J. Kenneth Tan,

and Jack J. Dongarra (Springer Berlin Heidelberg, Berlin, Heidelberg, 2002), p. 342.

[22] J. Villasenor and O. Buneman, Rigorous charge conservation for local electromagnetic field solvers, Comput. Phys. Commun. **69**, 306 (1992).

[23] T. Zh. Esirkepov, Exact charge conservation scheme for particle-in-cell simulation with an arbitrary form-factor, Comput. Phys. Commun. **135**, 144 (2001).

[24] Exploiting multi-scale parallelism for large scale numerical modelling of laser wakefield accelerators, Plasma Phys. Control. Fusion **55**, 124011 (2013).

[25] The multi TW few cycle OPCPA systems, https://ekspla.com/products/ultraflux-custom-multi-tw-few-cycle-opcpa-systems/.

[26] P. Sprangle and E. Esarey, Interaction of ultrahigh laser fields with beams and plasmas, Phys. Fluids B **4**, 2241 (1992).

[27] K. V. Lotov, Acceleration of positrons by electron beam-driven wakefields in a plasma, Phys. Plasmas **14**, 023101 (2007).

[28] M. J. Hogan, C. E. Clayton, C. Huang, P. Muggli, S. Wang, B. E. Blue, D. Walz, K. A. Marsh, C. L. O'Connell, and S. Lee, *et al.*, Ultrarelativistic-Positron-Beam Transport Through Meter-Scale Plasmas, Phys. Rev. Lett. **90**, 205002 (2003).

[29] J. J. Su, T. Katsouleas, J. M. Dawson, and R. Fedele, Plasma lenses for focusing particle beams, Phys. Rev. A **41**, 3321 (1990).

[30] S. Lee, T. Katsouleas, R. G. Hemker, E. S. Dodd, and W. B. Mori, Plasma-wakefield acceleration of a positron beam, Phys. Rev. E **64**, 045501 (R) (2001).

[31] E. Esarey, C. B. Schroeder, and W. P. Leemans, Physics of laser-driven plasma-based electron accelerators, Rev. Mod. Phys. **81**, 1229 (2009).

[32] W. Lu, M. Tzoufras, C. Joshi, F. S. Tsung, W. B. Mori, J. Vieira, R. A. Fonseca, and L. O. Silva, Generating multi-GeV electron bunches using single stage laser wakefield acceleration in a 3D nonlinear regime, Phys. Rev. ST Accel. Beams **10**, 061301 (2007).

[33] S. Corde, K. Ta Phuoc, G. Lambert, R. Fitour, V. Malka, A. Rousse, A Beck, and E. Lefebvre, Femtosecond x rays from laser-plasma accelerators, Rev. Mod. Phys. **85**, 1 (2013).

[34] R. Lehe, C. B. Schroeder, J.-L. Vay, E. Esarey, and W. P. Leemans, Saturation of the Hosing Instability in Quasi-linear Plasma Accelerators, Phys. Rev. Lett. **119**, 244801 (2017).

[35] P. Muggli, B. E. Blue, C. E. Clayton, F. J. Decker, M. J. Hogan, C. Huang, C. Joshi, T. C. Katsouleas, W. Lu, and W. B. Mori, *et al.*, Halo Formation and Emittance Growth of Positron Beams in Plasmas, Phys. Rev. Lett. **101**, 055001 (2008).

[36] A. Döpp, C. Thaury, E. Guillaume, F. Massimo, A. Lifschitz, I. Andriyash, J.-P. Goddet, A. Tazfi, K. Ta Phuoc, and V. Malka, Energy-Chirp Compensation in a Laser Wakefield Accelerator, Phys. Rev. Lett. **121**, 074802 (2018).

[37] Dataset of positron trapping and acceleration results when changing initial parameters. See https://doi.org/10.5281/zenodo.7817408.

[38] I. Dolev, I. Kaminer, A. Shapira, M. Segev, and A. Arie, Experimental Observation of Self-Accelerating Beams in Quadratic Nonlinear Media, Phys. Rev. Lett. **108**, 113903 (2012).